1 **Asymmetry in Three-Site Relaxation-Exchange NMR**

3 Bernhard Blümich,[1] Matthew Parziale,[2] and Matthew Augustine[2]

4 [1] Institut für Technische und Makromolekulare Chemie, RWTH Aachen University,

5 Worringer Weg 2, 52074 Aachen, Germany

6 [2] Department of Chemistry, UC Davis, One Shields Avenue, Davis, CA 95616, USA

8 Corresponding author: Bernhard Blümich, bluemich@itmc.rwth-aachen.de

10 Asymmetry of peak integrals in 2D relaxation maps of exchange between three sites

11 reports circular flow between the relaxation sites. This disagrees with detailed balance

12 according to which the exchange between any pair of sites must be balanced in

13 thermodynamic equilibrium. Confined diffusion of particles jumping randomly on a 2D

14 checkerboard grid to any of their eight neighbor positions and confined gas diffusion

15 were modelled in Monte Carlo simulations to explore the impact of topological

16 constraints on particle exchange between three pools. Both models produce density

17 variations across the pore and reveal that up to 1% of the molecules move in circular

18 paths between the relaxation pools. This motion is driven by different features of either

19 algorithm. It is silent in thermodynamic equilibrium, confirming that multisite exchange

20 maps are symmetric in this case. The coherent flux is argued to result from stochastic

21 pore resonance related to diffusion eigenmodes. If it can be driven experimentally by

22 external time-varying electric, magnetic or ultrasonic fields, this may be a way to

23 enhance heterogeneous catalysis.
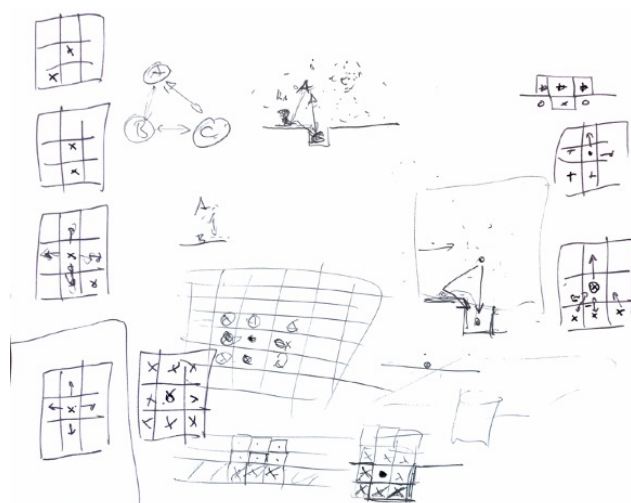
26 Graphical abstract: Draft of particle exchange on a 2D checkerboard grid

1. Introduction

Exchange is an essential ingredient of diffusion and spreading phenomena, which are abundant in nature and govern the evolution of tangible and intangible objects and goods (Bunde et al., 2018) as well as the physics of living systems (Gnesotto et al., 2018; Lynn et al., 2021). Nuclear Magnetic Resonance provides particularly powerful methodologies to investigate molecular exchange processes (Ernst et al., 1987; Callaghan, 2011). Slow molecular exchange on the millisecond time scale is studied by e. g. two-dimensional exchange NMR, i. e. by chemical exchange spectroscopy for rotational motion (Jeener et al., 1979) and by exchange relaxometry for translational motion (Lee et al., 1993). In equilibrium the nature of the exchange processes is commonly understood to be random Brownian motion, and the associated 2D NMR exchange maps are expected to be symmetric with respect to their diagonal. On the other hand, exchange in non-equilibrium leads to asymmetry. This has been observed in NMR, for example, in 2D chemical exchange spectra for chemical reactions involving different sites (Lacabanne et al., 2022), for the spread of hyperpolarization by spin diffusion (Björgvinsdóttir et al., 2021), for slow flow across porous media in relaxation exchange maps (Olaru et al., 2012), as well as in position- and velocity-exchange NMR (Han and Blümich, 2000).

The kinetics of transitions or exchange between discrete states driven by random processes are described by (van Kampen, 1992)

$$\frac{\mathrm{d}M_i(t)}{\mathrm{d}t} = \sum_j \{k_{ij}M_j(t) - k_{ji}M_i(t)\}, \tag{1}$$

where M_i are populations represented in NMR by magnetization components collected in the vector $\boldsymbol{M}$, and k_{ij} are the exchange rates equivalent to the transition probabilities from state j to state i, which are collected in the kinetic exchange matrix $\mathbf{k}$. In equilibrium

$$\frac{\mathrm{d}M_i(t)}{\mathrm{d}t} = 0, \tag{2}$$

and the number of all particles arriving at site i from sites j is equal to the number of all particles leaving from site i to sites j so that the total mass is conserved.

As a result of mass balance, two-site exchange between states or sites A and B always leads to symmetric 2D NMR exchange maps in thermodynamic equilibrium as the number $k_{\mathrm{BA}}M_{\mathrm{A}}$ of particles populating site B by leaving site A per unit time is equal to the number of particles $k_{\mathrm{AB}}M_{\mathrm{B}}$ leaving site B and populating site A per unit of time. This number is the product of the rate k_{BA} for transitions from site A to site B

60   times the population M_A of site A. The relationship $k_{BA}M_A = k_{AB}M_B$ is known as the

61   'principle of detailed balance'. In thermal equilibrium it is understood to also apply to

62   rate processes involving more than two sites (Onsager 1931, Gnesotto et. al. 2018).

63   By example of mass-balanced equilibrium diffusion between three sites

64   (Onsager 1931, Sandstrom, 1983), Eqn. (1) becomes

65   $$k_{21}M_1 + k_{31}M_1 = k_{12}M_2 + k_{13}M_3,$$

66   $$k_{12}M_2 + k_{32}M_2 = k_{21}M_1 + k_{23}M_3, \tag{3}$$

67   $$k_{13}M_3 + k_{23}M_3 = k_{31}M_1 + k_{32}M_2,$$

68   or equivalently, mass balance requires

69   $$k_{31}M_1 - k_{13}M_3 = k_{12}M_2 - k_{21}M_1 = k_{23}M_3 - k_{32}M_2. \tag{4}$$

70   Normalization of this expression to the total number of exchanges per unit time defines

71   the asymmetry parameter a_{sy} used below,

72   $$(k_{23}M_3 - k_{32}M_2)/[(1,1,1)\,\mathbf{k}\,\boldsymbol{M}] \stackrel{\text{def}}{=} a_{sy}. \tag{5}$$

73   Here $k_{ij}M_j$ is the number of transitions from pool j to pool i, corresponding to the peak

74   integral in an exchange map after correction for relaxation effects, so that the

75   denominator corresponds to the integral over all peaks. The asymmetry parameter

76   thus quantifies the imbalance of exchange between two sites in terms of the number

77   of unbalanced exchanges normalized to the total number of exchanges. Therefore, it

78   specifies the relative flux in the circular exchange process. While mass balance (4) is

79   a necessary condition for dynamic equilibrium, detailed balance, on the other hand, is

80   a stronger condition applicable to thermodynamic equilibrium. It requires

81   $$a_{sy} = 0. \tag{6}$$

82   Detailed balance had been introduced by Maxwell in 1867 based on 'sufficient

83   reason' in his derivation of the speed distribution of gas atoms considering the speed

84   exchange between colliding gas atoms in thermodynamic equilibrium (Maxwell, 1867).

85   An intriguing consequence of the exchange being balanced in detail between particles

86   A and B amounts to the impossibility of assigning positive time to either velocity

87   exchange from A to B or B to A on the particle scale of the exchange process, thus

88   admitting negative time or time reversal. In 1872 Boltzmann showed in an elaborate

89   treatment, that Maxwell's speed distribution also applies to polyatomic gas molecules

90   (Boltzmann, 1872). Furthermore, in 1917 Einstein derived Planck's law of black-body

91   radiation as a balanced energy exchange between quantized radiation and matter

92   underlining the striking similarity to Maxwell's speed distribution of gas atoms (Einstein,

93   1917). He concludes "Indem Energie und Impuls aufs engste miteinander verknüpft

94   sind, kann deshalb eine Theorie erst dann als berechtigt angesehen werden, wenn

95   gezeigt ist, daß die nach ihr von der Strahlung auf die Materie übertragenen Impulse

96   zu solchen Bewegungen führen, wie sie die Wärmetheorie verlangt," (Since energy

97   and momentum are intimately connected, a theory can only then be considered

98   justified, when it has been shown, that according to it the momenta of the radiation

99   transferred to the matter lead to such motions as demanded by the theory of heat.)

100   In his work extending Maxwell's speed distribution to polyatomic gas molecules

101   Boltzmann considered molecules in a container whereby the walls reflect the

102   molecules like elastic balls: "Bezüglich der Gefäßwände, welche das Gas

103   umschließen, will ich jedoch voraussetzen, dass die Moleküle an denselben wie

104   elastische Kugeln reflektiert werden. … Die Wände stören nicht, da an ihnen die

105   Moleküle wie elastische Kugeln reflektiert werden; also geradeso von ihnen

106   zurücktreten, als ob der Raum jenseits der Wände von gleich beschaffenem Gase

107   erfüllt wäre." (Concerning the container walls which enclose the gas, I want to presume

108   that the molecules are reflected from them like elastic balls. …. The walls do not

109   interfere, because the molecules are reflected from them like elastic balls; that is,

110   recede from them just like that, as if the space beyond the walls would be filled with

111   similarly conditioned gas.) Moreover, the interaction between gas molecules can be of

112   any type. While Boltzmann states that any other interaction between walls and

113   molecules leads to the same result albeit at loss of simplicity, the perfectly elastic

114   reflections of the gas molecules at the walls eliminate the topological constraints of the

115   box on their motion. For confined particles, this means that the pressure across the

116   pore volume is constant, i. e. the time average of the particle density does not vary

117   with the location inside the pore. Boltzmann obtained the same speed distribution for

118   polyatomic molecules with internal degrees of freedom as Maxwell had for atoms

119   based on detailed balance of speed exchange. In the simulations reported below, the

120   motion of molecules is considered for which the interactions with the walls are the

121   same as those among the molecules. Understanding confined diffusion (Valiullin,

122   2017) is important from a general point of view because the motion of molecules

123   without topological constraints is an ideal limit which cannot perfectly be realized in

124   practice although it may be realized within experimental uncertainty.

125   Two-site exchange processes will always be symmetric in equilibrium. This

126   situation has been evaluated analytically for NMR relaxation exchange of fluids in

127   porous media (McDonald, 2005). Yet multi-site relaxation-exchange NMR maps (Van

128 Landeghem, 2010) can formally be asymmetric in equilibrium. For example, the

129 transverse magnetization $s(t_1, t_2)$ from a three-site T_2-T_2 relaxation exchange NMR

130 experiment (Gao and Blümich, 2020),

131 $$s(t_1, t_2) = (1,1,1)e^{-(\mathbf{R}_2+\mathbf{k})t_2}e^{-(\mathbf{R}_1+\mathbf{k})t_\mathrm{m}}e^{-(\mathbf{R}_2+\mathbf{k})t_1}\boldsymbol{M}(t_0), \qquad (7)$$

132 has been simulated to model an experimentally observed asymmetric three-site T_2-T_2

133 NMR exchange map of water molecules saturating Al_2O_3 powder with the three

134 relaxation sites corresponding to bulk water, water molecules on the surface of the

135 powder particles and water molecules inside the surface pores (Fig. 1). Here $\boldsymbol{M}(t_0)$ is

136 the initial vector of transverse magnetization components from relaxation sites 1, 2 and

137 3 generated from longitudinal thermodynamic equilibrium magnetization with a 90°

138 pulse at the beginning of the experiment at time t_0, and t_1, t_m, t_2 are the evolution,

139 mixing, and detection time intervals of the 2D NMR experiment, respectively

140 (Callaghan, 2011; Lee et al., 1993). Apart from the relaxation-rate matrices $\mathbf{R}_1$ and $\mathbf{R}_2$,

141 and the kinetic matrix $\mathbf{k}$, the best match obtained by forward simulation returned the

142 peak integrals revealing an asymmetry parameter of $a_\mathrm{sy} = -1.2\%$. This asymmetry of

143 the forward and backward particle jumps between two sites specifies the relative

144 circular flux between the three sites (Fig. 1).

145
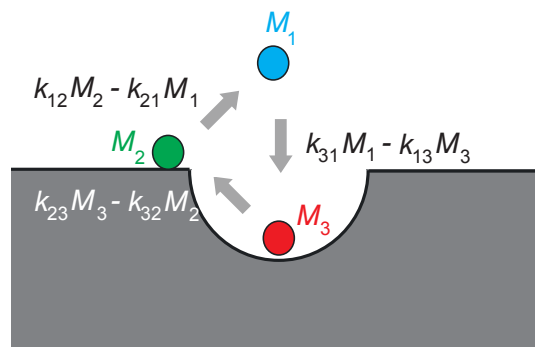
146
147 Figure 1. Asymmetry in three-site diffusion-mediated exchange indicates coherent
148 circular motion in a model example of water molecules in contact with a porous surface.
149 Three water populations M_j are identified by different NMR relaxation times and color.
150 They are molecules in the bulk (1), molecules on the surface (2) and molecules in the
151 pores (3). The exchange rate constants are k_{ji}. The net particle flux $k_{ij}M_j - k_{ji}M_i$
152 between two sites differs from zero. The net mass of all molecules participating in the
153 exchange is conserved. The figure illustrates positive a_sy.

154

155 The asymmetry observed in the experiment can be argued to result from the

156 uncertainty of the measurement and the data processing by 2D inverse Laplace

157 transformation (Song 2002). Also, asymmetric three-site exchange disagrees with

158 detailed balance of the exchange between any pair of sites in thermodynamic
159 equilibrium because it needs to be explained by circular diffusion on the pore scale,
160 and such motion resembles that of a rachet which Feynman has argued to disagree
161 with the second law of thermodynamics (Feynman et al., 1966). Nevertheless, Monte
162 Carlo simulations were executed and are discussed below to investigate asymmetry in
163 three-site exchange.

164

165 **2. Modelling confined diffusion**

166 **2.1 Vacancy diffusion: Random particle jumps on a 2D checkerboard**

167 Random jumps of particles from occupied sites to vacant sites were simulated with a
168 Monte-Carlo algorithm (Metropolis et al., 1953; Grebenkov, 2011; Hughes, 1995;
169 Sabelfeld, 1991) in a confined space on a checkerboard. The algorithm models
170 vacancy diffusion (Seitz, 1948) encountered in metals and alloys but the particles
171 perform the jumps rather than the vacancies. To keep the simulation simple, it is limited
172 to jumps on a 2D 3×3 Moore lattice of range 1 (Wolf-Gladrow, 2000) following rules of
173 the game of life (Wolf-Gladrow, 2000; Bialnicki-Birula, 2004). Here the center particle
174 can jump to any of its 8 neighbors (Fig. 2). Different neighborhoods of range 1 were
175 tested (Fig. S1) (Bialnicki-Birula, 2004), but only the Moore neighborhood having the
176 highest symmetry of all neighborhoods, produced data consistent with Eqn. (4).
177 Topological constraints are introduced which set boundaries to the jump space.
178 Initially, the available cells inside the jump space on the grid are populated randomly
179 with particles up to a specified particle density. Particles in the bulk are indexed 1, and
180 two distinct boundary sections are indexed 2 and 3, giving three environments for the
181 particles to be exposed to and between which randomly selected particles can move.
182 A particle jumping from environment j to i is counted by incrementing the element ij of
183 a 3×3 jump matrix with elements $k_{ij}M_j$ by 1. If the particle environment does not
184 change with the jump, the respective diagonal element $k_{jj}M_j$ is incremented. The NMR
185 relaxation environments are indexed according to increasing relaxation rate. If a
186 particle is in contact with two different relaxation environments, it is assigned to the
187 relaxation environment with the higher index according to the higher relaxation rate.
188   Different rules governing jumps to a neighbor cell were explored. 1) In the
189 simplest case, one of the 8 destination cells was chosen at random without assigning
190 a jump probability. When destination cell was free, the jump was executed, and the
191 initial and final environments were compared to increment the corresponding entry in

the jump matrix accordingly. When the destination cell was occupied, the particle remained at its source cell, and the respective diagonal element of the jump matrix was incremented. In all other cases, jump probabilities were assigned. 2) As a subtle variant of the random jumps to any of the 8 neighbor cells, jumps were randomly selected to any of the *free* neighbor cells by assigning zero jump probability to occupied neighbor cells and equal probability for jumps to the empty cells. This algorithm is known to violate detailed balance (Metropolis et al., 1953; Reviewer, 2023). 3) With reference to the Helmholtz free energy $A = U - T S$, where U is internal energy, T is temperature, and S is entropy, a jump probability $p = \exp\left\{-\frac{\Delta A}{k_\text{B} T}\right\}$ was introduced, where $\Delta A = \Delta U - T \Delta S$, T is the temperature, and k_B the Boltzmann constant. $\Delta U = -\boldsymbol{F} \Delta \boldsymbol{R}$ and ΔS were estimated from the sum of distances to free or occupied neighbor cells by crude empirical models as detailed in the supporting information. Here $\boldsymbol{F}$ is the force and $\Delta \boldsymbol{R}$ the distance vector between two particles. This allowed probing attractive and repulsive interactions by changing the sign of ΔU in simulation runs and varying temperature in addition to varying population density equivalent to pressure. It is noted here that the force field on a randomly populated lattice is not conservative (Reviewer, 2023). In other words, the energy balance of a particle moving in a circle is different from zero, and Monte Carlo simulations under these constraints probe a driven equilibrium and not thermodynamic equilibrium (Michel et. al., 2014).

Figure 2. Jumps on a checkerboard grid modelling vacancy diffusion. The center particle can jump to any of its eight next nearest neighbor cells, which are numbered clockwise from 1 to 8. Jump probabilities were introduced to account for particle interaction between the center particle (red) and neighbor particles (black).

The vacancy-diffusion simulations were carried out with a program written in Matlab R2020a by The MathWorks Inc. on an Apple MacBook Pro 2.4 GHz having an Intel Quad-Core i5 processor. Unless indicated otherwise, 10^7 jumps were simulated in one run taking 75 seconds.

2.2 Gas diffusion

The gas diffusion calculations explore similar pore size and occupancy. Here the motion of circular particles with diameter equal to the cell size was accomplished by propagating an initial distribution of particle speeds for random initial positions and directions in a Monte Carlo fashion based on instantaneous collisional forces. This distribution rapidly equilibrated to a Maxwell-Boltzmann distribution. Whereas in vacancy-diffusion simulations the distribution of particles in the pore is recorded after each jump it is recorded in the gas-phase simulations at constant time intervals. If the center of each particle was within one diameter of another, the particles are considered to have collided. Immediately after a collision the projection of the velocity vector along the collision axis is reversed prior to propagating to the next step. In this approach, the observation time interval must be sufficiently small, so that the new velocities are calculated with a small position uncertainty of the colliding particles (Reviewer 2023, Michel et al. 2014).

The collisions change both the direction and velocity of the particles at each of the 10^9 constant time increments used here. Following conservation of momentum and kinetic energy,

$$\vec{v}_{1,\text{new}} = \vec{v}_{1,\text{old}} - \frac{2m_2}{(m_1+m_2)} \frac{\langle \vec{v}_{1,\text{old}} - \vec{v}_{2,\text{old}}, \vec{x}_1 - \vec{x}_2 \rangle}{\|\vec{x}_2 - \vec{x}_1\|^2} (\vec{x}_1 - \vec{x}_2), \tag{8}$$

$$\vec{v}_{2,\text{new}} = \vec{v}_{2,\text{old}} - \frac{2m_1}{(m_1+m_2)} \frac{\langle \vec{v}_{2,\text{old}} - \vec{v}_{1,\text{old}}, \vec{x}_2 - \vec{x}_1 \rangle}{\|\vec{x}_2 - \vec{x}_1\|^2} (\vec{x}_2 - \vec{x}_1). \tag{9}$$

These collisions with other particles and the wall are mediated by the particle size, which is set to be a fraction of the pore-side length of one. This means that a square pore with a five-particle diameter side length is populated with particles having a diameter of 1/5. To compare the continuous positional output of this model to vacancy diffusion, a two-dimensional square grid with cell size set by the particle diameter is imposed on the entire pore. The quasi-continuous positional output is then binned into these cells and compared to the binned positions from the previous observation to determine if particles translated between the main pore volume, pore wall, and active site. The translational information is used to assign estimates of the jump-matrix elements and thus the asymmetry parameter a_{sy}.

The gas-diffusion simulations were carried out with a program written in Matlab R2020a by The MathWorks Inc. on a home-built desktop computer possessing an AMD R y z e n 7 2 7 0 0 processor. In most cases, 10^9 jumps were simulated in one run taking roughly 45 hours to complete.

256

3. Results

257

Two different pore geometries were analyzed. Initially, the simulation was executed for

258

a pore geometry (Fig. 3a) which approximates the surface structure of Fig. 1, and

259

which is hypothesized to explain the observed asymmetry of water diffusing in a porous

260

Al_2O_3 grain pack (Gao and Blümich, 2020). The dented surface was mirrored

261

horizontally to double the probability of particles entering the dent (relaxation site 3) in

262

the otherwise straight surface (relaxation site 2). The bulk of the particles defines

263

relaxation site 1. Periodic boundary conditions were employed right and left. A pore

264

boundary has been treated just like an occupied cell with the same rules applying to

265

the jump probability. The simulations of particle motion confined to this complex pore

266

structure and constrained by jump probabilities revealed the existence of asymmetric

267

exchange. To understand the essence of the asymmetry the pore geometry was

268

simplified to a square with an active site in the wall to study particle motion in detail.

269

Particles in the bulk, in contact with the walls, and with the active site are identified by

270

different NMR relaxation properties (Fig. 3b).

271

272

a)   b)

273
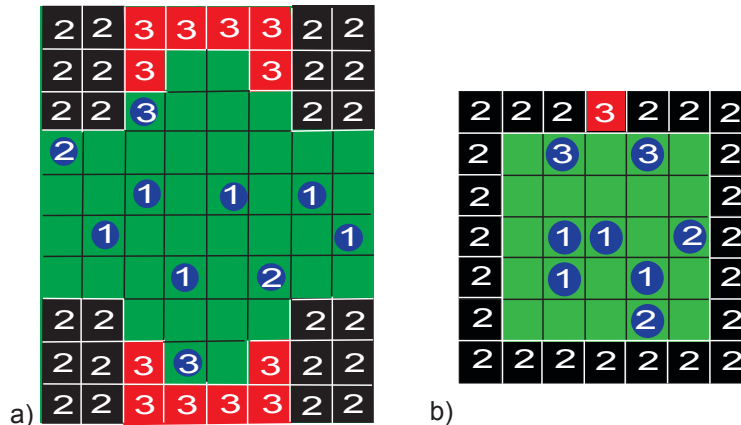
Figure 3. Examples of pore models for two-dimensional three-site exchange based on
a checkerboard grid. Particles can occupy one cell and jump to a neighboring one
following different realizations of the jump probability. a) Porous solid. The boundaries
right and left are periodic. The boundaries top and bottom are rigid. Depending on their
next neighbors in the first coordination shell, the particle-relaxation environments are
identified as bulk (1), surface (2), and pore (3) with increasing relaxation rate. b) Small
square pore with an active site. The bulk (1), the walls (2), and the active site (3) have
different relaxation properties. If a particle is in contact with two different relaxation
sites, it is counted to belong to the particle pool with the larger relaxation rate, i. e. the
pool with the higher number.

284

285

Enabled by the interaction model, which, depending on the particle environment

286

assigns different jump probabilities as a function of temperature, the asymmetry

287   parameter a_{sy} was evaluated for both pores with the vacancy-diffusion algorithm as a
288   function of temperature T and pressure P. Pressure was varied in terms of the
289   population density measured as the fraction of cells occupied in the pore. The results
290   for the complex pore are reported in the supplementary material (Fig. S3), whereas
291   those for the simple square pore are reported in the main text here (Fig. 4). At certain
292   temperatures and pressures also the autocorrelation function of the occupation-time
293   track of a particular cell and its Fourier transform were determined. Striking features
294   observed in vacancy diffusion were subsequently modelled with the gas-diffusion
295   algorithm in the square pore.

296

297
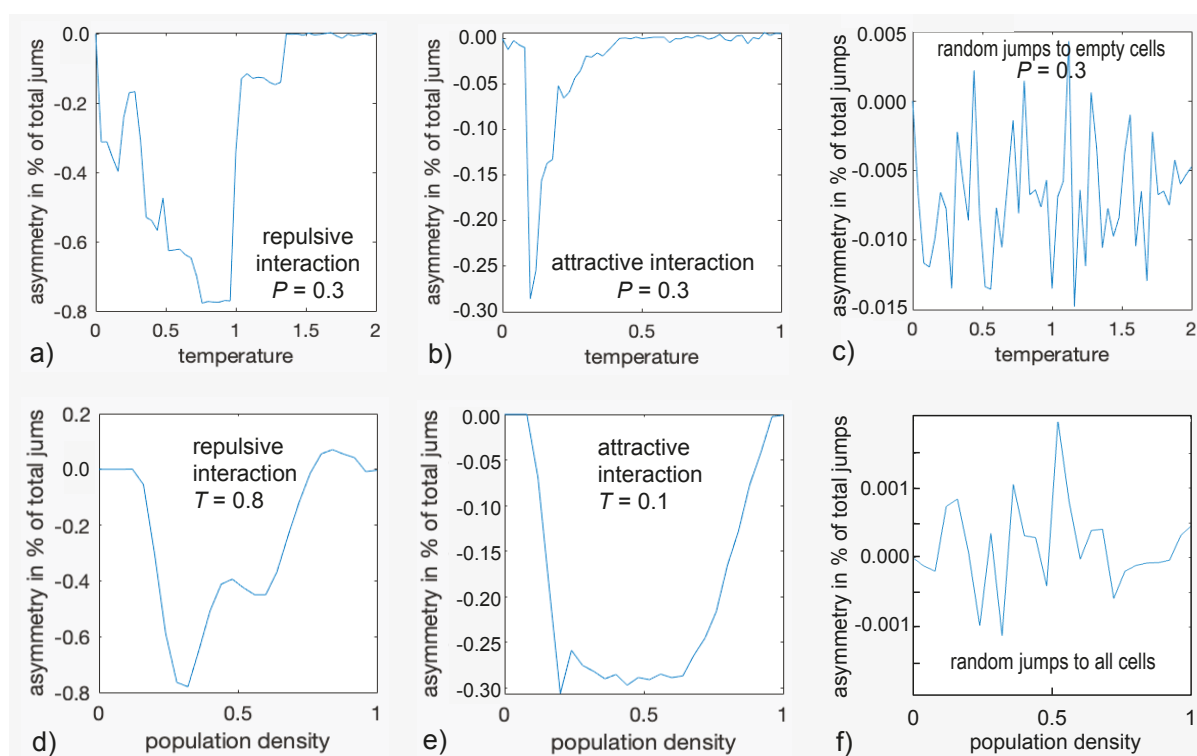
298   **Figure 4**. Asymmetry parameters a_{sy} for diffusion inside the small rectangular pore
299   depicted in Fig. 3b as a function of temperature T (a-c) and pressure P (d-f). a) $a_{\mathrm{sy}}(T)$
300   for repulsive interaction at $P = 0.3$. b) $a_{\mathrm{sy}}(T)$ for attractive interaction at $P = 0.3$.
301   c) $a_{\mathrm{sy}}(T)$ for jumps to randomly selected empty cells. d) $a_{\mathrm{sy}}(P)$ for attractive interaction
302   at $T = 0.8$. e) $a_{\mathrm{sy}}(P)$ for attractive interaction at $T = 0.1$. f) $a_{\mathrm{sy}}(P)$ for jumps to cells
303   randomly selected from all eight neighbor cells.

304

305   Relevant results for the square pore (Fig. 3b) are summarized in six graphs in
306   Fig. 4. The asymmetry parameter varies strongly with temperature T (Figs. 4a,b) and
307   pressure corresponding to population density P (Figs. 4d,e). All parameters are relative
308   quantities without units. The top three graphs a), b) and c) show the variation of a_{sy}
309   with temperature for a population fraction of 0.3 corresponding that of a gas. The

310   asymmetry parameter assumes only negative values in an abrupt but reproducible

311   manner in the range of -0.8% < a_{sy} < 0.0% for repulsive interaction (Fig. 4a), i. e. for

312   the definition of the force between particles as illustrated in Fig. S2a. With reference to

313   Fig. 1, negative a_{sy} reports that the straight exit route from the active site towards the

314   center of the pore is preferred over the detour via the pore wall. When the interaction

315   is changed from repulsive to attractive by inverting the sign of ΔU in the expression for

316   the free energy, the asymmetry parameter varies as well, however, only between -

317   0.3% < a_{sy} < 0.0% (Fig. 4b). In either case, the asymmetry parameter varies with

318   temperature and pressure. It is concluded, that for this small pore, up to about 1% of

319   all jumps on the checkerboard can proceed in an ordered circular fashion between the

320   three sites. Similar behavior is observed for the complex pore of Fig. 3a as illustrated

321   in Fig. S3 in the supplement.

322   At the extrema of the $a_{sy}(T)$ curves in Figs. 4a,b the dependence of the

323   asymmetry parameters on population density was investigated (Figs. 4d,e). The

324   variations with population density are smoother than those with temperature.

325   Significant negative asymmetry results at intermediate pressure, while at low and high

326   pressure, the asymmetry is small (Fig. 4d,e). At higher temperature and high pressure,

327   small positive a_{sy} is observed (Fig. 4d, T = 0.8, P = 0.8). If the destination cell for a

328   jump is chosen at random without considering a hypothetical free jump energy A,

329   essentially noise more than two orders of magnitude smaller is observed for the

330   exchange asymmetry determined from 10^7 jumps when varying T and P (Fig. 4c,f).

331   However, a small bias towards negative a_{sy} results if the destination cell is chosen at

332   random from all fee neighbor cells (Figs. 4c), whereas no bias is detected if the

333   destination cell is chosen at random from all neighbor cells whether free or occupied

334   (Fig. 4f). This difference becomes more pronounced at higher number of jumps (see

335   below).

336   To shed further light on the origin of the asymmetry, autocorrelation functions of

337   the occupation-time tracks of selected cells in the pore were computed and Fourier

338   transformed (Fig. 5). The occupation-time track was calibrated to zero mean for purely

339   random occupation, i. e. it contained the negative population density when it was empty

340   and the complement of the population density to one when the cell was occupied. The

341   faster the autocorrelation function decays, the less coherent the cell population

342   fluctuates and the broader is its Fourier transform, i. e. the transfer function (Fig. 5b,c).

343   A constant offset of the autocorrelation function shows that the time-average

344   population in the cell differs from the mean population of the pore (Fig. 5a,b). This
345   offset produces a spike at zero frequency in the transfer functions. Subtracting the
346   offsets from the autocorrelation functions and scaling the resulting functions to the
347   same amplitude reveals different decays in different cells and thus variations in particle
348   dynamics across the pore (inset in Fig. 5c, middle). These dynamics cannot readily be
349   measured for a single cell in the pore, although an average over all cells and pores in
350   the measurement volume would be amenable to experiment by probing the particle
351   dynamics with CPMG measurements in magnetic gradient fields at variable echo time.
352   Such measurements provide the frequency-dependent diffusion coefficient in terms of
353   the Fourier transform of the velocity autocorrelation function (Stepišnik et al., 2014,
354   Callaghan and Stepišnik, 1995; Parsons et al., 2006).

355
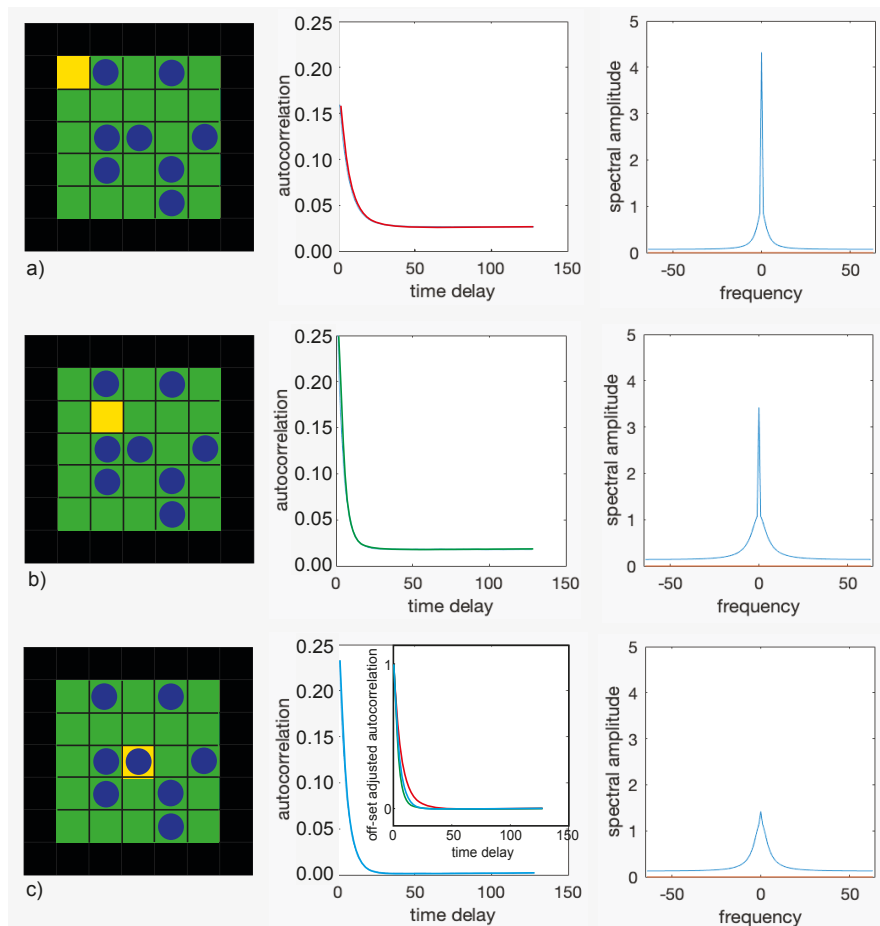
356

357   Figure 5. Autocorrelation functions (center) of the occupancy of the yellow cells (left)
358   and the real parts of their Fourier transforms (right) for repulsive interaction at $T = 0.1$
359   and $P = 0.3$. a) Corner cell. b) Off-center cell. c) Center cell. The inset in the middle
360   compares the decays of all three autocorrelation functions after subtraction of the
361   offsets.

362

363
a) b) c) d) e) f) g)
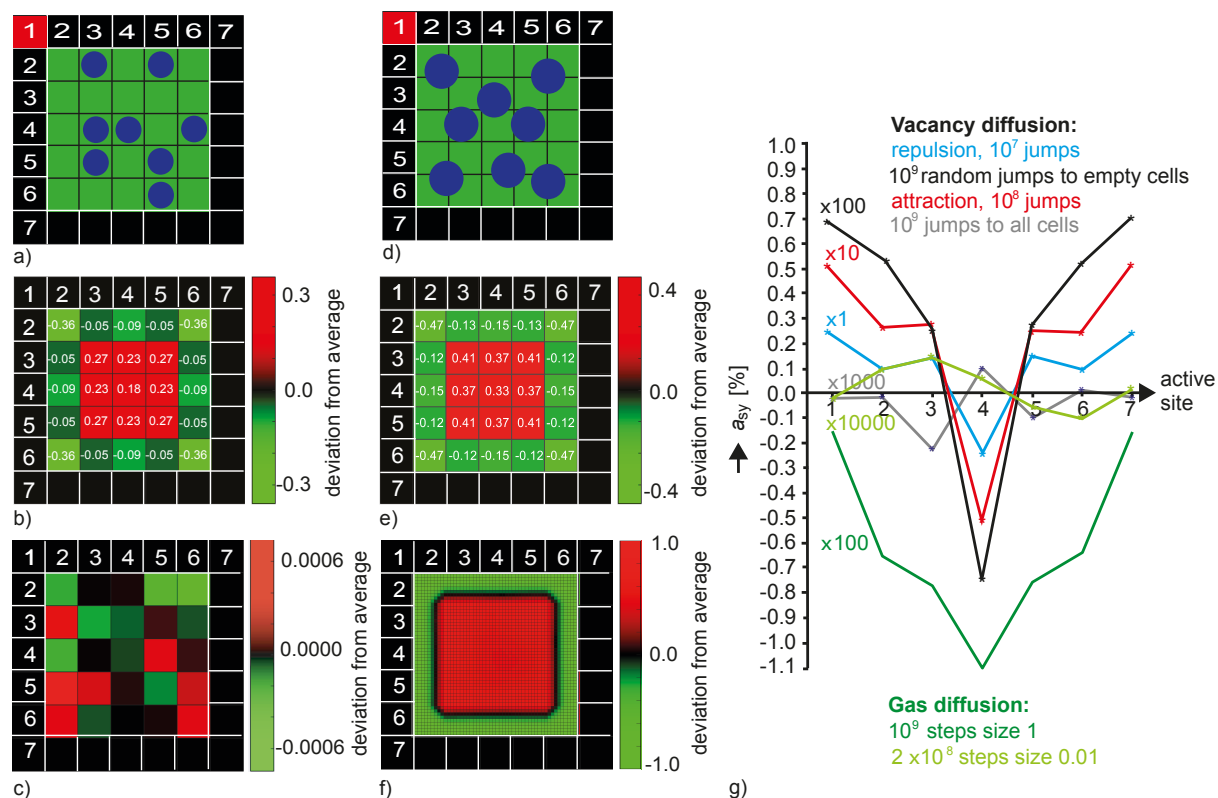
364 **Figure 6.** Population density distributions and dependences of the asymmetry
365 parameter a_{sy} on the position of the active relaxation site in the wall of a pore with 5 ×
366 5 cells. a) Vacancy diffusion. Particles can jump one step on the grid in 8 directions.
367 b) Deviations from average relative density 1 for 10^9 jumps chosen at random to any
368 of the free neighbor cells. c) Deviations from average relative density 1 for 10^9 jumps
369 chosen at random to any of the 8 neighbor cells. d) Gas diffusion. The particle motion
370 is computed on a fine grid. e) Deviations from average relative density 1 for 10^9
371 observations of particle positions at observation intervals of duration 1. The particle
372 position at the time of observation is binned to the course vacancy-diffusion grid.
373 f) Deviations from average relative density 1 on a fine 50×50 grid of 0.1 particle
374 diameters for 10^9 observations of particle positions at observation intervals of duration
375 0.01. g) Variations of the asymmetry parameter with the position of the active site in
376 the cell wall for differently interacting particles for vacancy diffusion at $T = 0.2$, $P = 0.3$,
377 and different jump probabilities as well as for gas diffusion at long and short
378 observation intervals of 1 vs. 0.01. The mirror symmetry of each trace about the center
379 position reports high precision of the simulation.

380

381   While the autocorrelation function is difficult to probe experimentally, the

382 asymmetry parameter a_{sy}, on the other hand, probes the particle dynamics and could

383 be investigated experimentally directly by relaxation-exchange NMR experiments

384 provided the signal-to-noise ratio is good enough. The parameter depends on the

385 location of the relaxation center in the pore wall (Fig. 6). This dependence has been

386 verified to be identical for all walls of the square pore. Moreover, it exhibits mirror

387 symmetry about the center position (Fig. 6g), assuring that the simulation noise is

388 negligible. For vacancy diffusion in a 5 × 5 square pore with walls 7 cells wide (Fig.

389   6a,b), a_{sy} varies consistently with position when the jumps are selected following *a*

390   *priori* defined probabilities, irrespective of the particle interaction being positive,

391   negative, or the destination cell having been chosen randomly from all free neighbor

392   cells. But the magnitude of a_{sy} depends strongly on the selection rule defined by the

393   jump probability as indicated in Fig. 6g by the scaling factors. It is highest at the corner

394   positions and lowest at the center position. For random jumps to empty cells, a_{sy} is

395   more than an order of magnitude smaller than for repulsive interaction, so that the

396   number of particle jumps had to be increased to 10^9 resulting in 3 h computation time

397   for each data point in the corresponding trace (black) Fig. 6e. Interestingly, for gas

398   diffusion (Fig. 6d) a_{sy} varies at long observation interval (green, Fig. 6g) in a fashion

399   similar to that for vacancy diffusion, is of magnitude comparable to that of vacancy

400   diffusion (black, Fig, 6g), but does not change sign with position of the active site in

401   the pore wall. In all these cases the precision of the asymmetry parameter a_{sy} obtained

402   in the simulations exceeds the second relevant digit. If the jumps in the vacancy

403   diffusion simulations are chosen without bias from a jump probability no exchange

404   asymmetry is detected, only noise nearly more than one order of magnitude lower than

405   for jumps selected at random to one of the free neighbor positions (grey, Fig. 6g).

406   Similarly, the asymmetry parameter decreases with the observation time becoming

407   shorter by more than two orders of magnitude as illustrated in Fig. 6g for a long time

408   step of 1 (dark green) versus a short time step of 0.01 (light green) in simulation units

409   of $(m\ s^2\ /k_B T)^{1/2}$.

410   The particle dynamics manifested in a_{sy} are accompanied by variations of the

411   average population density across the pore which is depleted in the contact layer of

412   the particle with the pore wall, enhanced in the next layer, and tapers off towards the

413   pore center in both cases (Figs. 6b,e, Fig. S4). The densities vary in a similar fashion

414   across the pore for both types of diffusion albeit having somewhat different values as

415   can be verified by close inspection of the numbers in each cell in Figs. 6b,e. These

416   density variations disagree with Boltzmann's argument, that elastic collisions with the

417   walls effectively remove the impact of the walls to the effect, that the walls can be

418   neglected. Agreement, however, is reached, if the destination cells for particle jumps

419   in vacancy diffusion are chosen at random from all and not just the free neighbor cells

420   (Fig. 6c; Metropolis et al., 1953). Shortening the observation interval in the gas-

421   diffusion simulations, however, maintains the unphysical density distribution across the

422   pore and has no effect due to binning the particle positions to the vacancy-diffusion

423   grid at the time of observation, as the exact moment of a particle collision cannot be

424   determined on a discrete time axis. On a finer grid, however, the population density is

425   homogeneous except for the regions close to the walls, which the center of the circular

426   particles cannot approach (Fig. 6f). If, however, projected onto the course vacancy-

427   diffusion grid the population-density modulations (Fig. 6e) reappear, because the exact

428   locations of collisions cannot be determined in a simple way at finite observation-time

429   intervals. Nevertheless, for both algorithms, the asymmetry parameter approaches

430   zero for all positions along the wall of the square pore (Fig. 6g, light green), confirming

431   that detailed balance is observed.

432   The maps in Fig. 6b,c,e,f revealing the deviation of local population density from

433   average population density were calculated by summing the 2D maps of particle

434   locations after each jump or at each observation time, normalizing the resultant maps

435   to the number of jumps and the particle density and subtracting the average mean

436   expected for a constant particle density across all cells in the pore. Further maps of

437   population density variations for the two different pores of Fig. 3 with other sizes and

438   interaction parameters are summarized in Fig. S4 of the supplement. While the particle

439   density varies less with temperature for vacancy diffusion, different density patterns

440   are found at different pressures. The strongest density variations are near the pore

441   wall whether the interaction is repulsive, attractive, or based on prior knowledge that a

442   neighbor cell is occupied. This becomes particularly evident for larger pores (Figs.

443   S4b,d,e). Coincidentally, at low density the main features of the density maps are

444   strikingly similar for vacancy diffusion with destination cells chosen randomly from

445   among the free neighbor cells (Figs. S4b) and gas diffusion (Figs. S4d). The particle

446   density is strongly depleted at the pore corners and near the wall and significantly

447   increased in the next particle layer (Figs. S4e,f). For interacting particles, this

448   concentration variation is carried forward in vacancy diffusion with increasing distance

449   from the wall leading to concentration waves which taper off towards the center of the

450   pore and interfere with each other coming from different directions. For small pores

451   interference patterns dominate the density distribution across the pore (Figs. 6b,e and

452   Figs. S4a,c). For particles jumping randomly to empty neighbor cells, the decay of the

453   concentration wave towards the pore center is fast with few to no oscillations towards

454   the pore center, while the oscillations are enhanced by conditioning the jump

455   probability with a hypothetical free jump energy (Fig. S4d, $P = 0.2$). In particular, the

456 population density at the active site in the dent of the complex pore of Fig. 3a depends

457 on the parameters P and T (Figs. S4a,b).

458

459 **4. Discussion**

460 Confined two-dimensional diffusion has been modelled by two different algorithms to

461 investigate in how far the cross-peaks in 2D T_2-T_2 exchange maps can be asymmetric.

462 The asymmetry is quantified by an asymmetry parameter a_{sy} which reports the relative

463 flux between two sites corresponding to the difference in the number of forward and

464 backward exchanges normalized to the total number of exchanges. The vacancy-

465 diffusion algorithm models particle jumps on a checkerboard grid to nearest neighbor

466 cells under the constraint of different jump probabilities and samples the population

467 map after each jump. The jump probability was determined from a Boltzmann

468 distribution with a heuristic free energy which depends on the populations of the

469 surrounding cells. The asymmetry parameters turned out to be equal to zero in the

470 case of equal jump probability to all neighbor cells (Metropolis et al., 1953), whether

471 occupied or not, confirming the validity of detailed balance (Fig. 6g). It was found to be

472 different from zero when different jump probabilities were assigned to different

473 neighbor cells, i. e. when the jump energy depended on the population pattern of the

474 neighbor cells. But with the statistical arrangement of the particles on a checkerboard

475 and the confinement of the interaction force to next nearest neighbors, energy is not

476 conserved with a particle move, so that each particle move either injects or extracts

477 energy from the system. Nevertheless, the equilibrium condition (3) is fulfilled, so that

478 the system is not in thermodynamical equilibrium but rather in an equilibrium that is

479 driven by the algorithm. The observed asymmetry parameter is, therefore, assigned to

480 a driven and not thermodynamic equilibrium.

481   The gas-diffusion algorithm models particles colliding with initial velocity vectors

482 and calculates new velocity vectors after a collision from conservation of energy and

483 momentum, whereby the instant of a collision is interrogated on a discrete time grid.

484 The smaller the observation time, the more precise the instant of a collision is

485 determined. Any deviation from the exact collision time leads to errors in the position

486 coordinates of the colliding particles and thus their velocities (Eqns. 7,8; Michel et al.

487 2014). While for large observation time a significant asymmetry parameter is observed

488 (Fig. 6g, dark green) its value shrinks drastically when the observation time is reduced

489 by a factor of 100 (Fig. 6g, light green). It is concluded that in the limit of infinitely short

490 observation time, also the gas-diffusion algorithm can produce vanishing asymmetry
491 parameter in three-site exchange in agreement with the principle of detailed balance
492 and with symmetry in the cross-peak intensities of exchange maps in thermodynamic
493 equilibtium. If, on the other hand, the velocities are calculated with a systematic error
494 in the gas-diffusion model due to a finite observation interval, the resultant velocities
495 disagree with the energy and momenta of elastic collisions, so that also here energy
496 is injected or extracted from the system and the observed asymmetry parameter can
497 be attributed to a driven and not a thermodynamic equilibrium.

498   The asymmetry parameters observed for either of the two pore shapes (Fig. 3)
499 investigated with the vacancy-diffusion model vary in a range on the order of $-1\% <$
500 $a_{\mathrm{sy}} < 1\%$, i. e., up to 1% of all particles in the pore do not follow detailed balance
501 between all pairs of sites but move coherently in circles between the three sites. It is
502 emphasized that this circular exchange is between the pools of particles representing
503 the three sites, and it is not a motion followed by individual particles completing circular
504 jumps. Given repulsive or attractive interaction in the vacancy diffusion model with
505 heuristic temperature and pressure dependent jump probabilities, the variations of a_{sy}
506 with temperature T appear rapid, reminiscent of phase transitions (Figs. 4a,b, Figs.
507 S3a). The variations of a_{sy} with pressure corresponding to population density P are
508 smooth (Figs. 4d,e, Figs. S3b). Either positive or negative values of a_{sy} are observed
509 as T or P change. A sign change of a_{sy} reports a change in the sense of the circular
510 exchange (cf. Fig. 1).

511   For a simple square pore, the asymmetry parameter varies with the position of
512 the active site in the cell wall, exhibiting mirror symmetry with respect to the wall center
513 (Fig. 6g). The variation is the same for the different jump probabilities, referred to as
514 repulsive and attractive interaction or random jumps to empty cells albeit it differs
515 significantly in magnitude. A similar dependence is observed in the gas-phase diffusion
516 simulations at long observation time. Moreover, the autocorrelations functions and
517 their Fourier transforms have been determined for the occupancy time tracks of
518 selected cells at specific positions inside a small square pore for 10^7 jumps of all
519 particles in the pore (Fig. 5). The time-track function had been devised to have zero
520 mean for the average cell population. Depending on the position of the cell inside the
521 pore, the autocorrelations functions and their Fourier transforms vary. Specifically, the
522 autocorrelation function can exhibit a significant constant offset. At these positions
523 inside the pore, the particle densities are different from the pore average, and the cell

524 is on average emptier or more occupied than expected if the exchange between all
525 cells were the same. This conclusion is supported by the observed deviations of the
526 cell occupancies from the pore average (Figs. 6b,e, Fig. S4). Near the pore wall the
527 average population density is depleted and varies in an oscillatory manner along the
528 pore wall. Further towards the center of the pore the average population density
529 increases sharply and then tapers off towards the pore center to a value slightly above
530 the average density.

531 These observations for driven vacancy diffusion in a square pore with 5×5 cells
532 are compared to independent simulations of driven gas diffusion (long observation
533 time: step size 1) of non-interacting particles in a square pore with an edge length of 5
534 particle diameters also allowing 7 relaxation centers along the pore wall (Figs. 6a,d).
535 A similar variation of the asymmetry parameter is found as for vacancy diffusion, but
536 the asymmetry parameter is negative for all positions of the active site (Fig. 6g, dark
537 green). Moreover, the depletion of the average particle density at the pore wall and its
538 subsequent variation towards the center are similar with the exception, that oscillations
539 of the average particle density along the pore wall are weaker for gas diffusion for the
540 (Figs. 6b,e). These oscillations persist even at short observation times due to the
541 uncertainty of localizing the particle positions at the exact time of their collision on a
542 discrete time grid. The lack of a sign change in the asymmetry parameter with changing
543 position of the active site may be explained by destructive interference of particle
544 collisions from multiple sites with the wall within one discrete particle diameter and the
545 fact, that the free path length between collisions in gas diffusion is not limited to the
546 next cell as in vacancy diffusion but can range up to the pore diameter. Taken together,
547 the observed asymmetry in the three-site exchange in driven equilibrium and the
548 variation of the jump statistics with position inside the pore point at diffusive resonance
549 phenomena like standing waves of air in pipes as reported by Kundt (Kundt, 1866) or
550 of vibrating plates as reported by Chladni (Chladni, 1787).

551 Three-site exchange can be viewed as a finite difference approximation to the
552 Laplace operator (van Kampen, 1992; Kuprov, 2022) governing Fick's second law
553 (Fick, 1855). Considering some local site *N* with neighbor sites *N*-1 and *N*+1 right and
554 left, the mass flow to and from site *N* given by Eqn. (1) is

555 $$\frac{\mathrm{d}m_N(t)}{\mathrm{d}t} = k_{N,N-1}m_{N-1} - k_{N-1,N}m_N + k_{N,N+1}m_{N+1} - k_{N+1,N}m_N, \tag{10}$$

556 Taking the limit to infinitesimal small distance $\Delta r \rightarrow \mathrm{d}r$ between the neighboring sites

557 leads to $k_{j,i} = k$, revealing that (10) is a finite difference approximation of a second

558 spatial derivative balanced by the temporal variations of m during infinitesimal time $\mathrm{d}t$,

559 $$(k\, m_{N-1} - 2\, k\, m_N + k\, m_{N+1})/\Delta r^2 \approx k\frac{\mathrm{d}^2 m}{\mathrm{d}r^2} = \frac{\mathrm{d}m}{\mathrm{d}t}/\Delta r^2. \tag{11}$$

560 In this limit, Eqn. (11) becomes Fick's second law with the diffusion coefficient $D =$

561 $k\Delta r^2$. This back-of-the-envelope argument suggests that the observed asymmetry of

562 three-site exchange is a property of Fick's second law and relates to igenmodes of the

563 Laplace operator (Hoop and Prange 2007, Grebenkov and Nguyen 2013).

564   The diffusion equation applicable to longitudinal magnetization in NMR instead of

565 particle masses m is the Bloch-Torrey equation (Torrey, 1956),

566 $$\frac{\partial}{\partial t}m(\boldsymbol{r},t) = D\boldsymbol{\nabla}^2 m(\boldsymbol{r},t) - \mu\, m(\boldsymbol{r},t), \tag{12}$$

567 where m now is the magnetization deviation from thermal equilibrium and μ is the bulk

568 relaxation rate. $m(\boldsymbol{r},t)$ solves this equation in terms of an expansion into normalized

569 eigenfunctions $\phi_n(\boldsymbol{r})$ with amplitudes A_n and eigenvalues τ_n (Brownstein and Tarr,

570 1977; Song, 2000)

571 $$m(\boldsymbol{r},t) = e^{-\mu t}\sum_{n=0}^{\infty} A_n\, \phi_n(\boldsymbol{r})\, e^{-\frac{t}{\tau_n}}. \tag{13}$$

572 The eigenvalues are determined by the boundary condition

573 $$D\,\boldsymbol{n}\,\boldsymbol{\nabla}\phi_n(\boldsymbol{r}) = \rho\,\phi_n(\boldsymbol{r}), \tag{14}$$

574 where ρ is the surface relaxivity and $\boldsymbol{n}$ is the unit vector normal to the surface. They

575 depend on the diffusion coefficient and determine the NMR relaxation time in different

576 ways according to the pore geometry. The population ϕ_0 of the lowest normal mode

577 has no nodes. The higher normal modes ϕ_n possess nodal surfaces. The higher

578 diffusion eigenmodes have been detected by NMR with selective excitation of partial

579 pore volumes making use of field gradients internal to the pore (Song, 2000). These

580 experimental results reported by Song agree with the Monte Carlo simulations of driven

581 diffusive translational motion in pores reported here, in that the population density

582 varies across the pore and that the offset of the autocorrelation function of the local

583 pore occupancy depends on the position of the cell in the pore. It needs to be

584 investigated further how much the NMR relaxation times and the associated particle

585 dynamics vary with the position from the pore wall to the center in the driven

586 concentration wave (Bytchenkoff and Rodts, 2011). On the other hand, stochastic

587 resonance in thermodynamic equilibrium has been observed with NMR first by Sleator,

588 Hahn et al. (Sleator et al., 1985) and subsequently studied in detail by Müller,

589   Jerschow, et al. in different scenarios (Müller and Jerschow, 2005; Schlagnitweit and

590   Müller, 2012). There, the magnetization fluctuating with the thermal motion of the

591   nuclear spins assumes the role of the particles and the resonance circuit assumes the

592   role of the pore. Diffusion eigenmodes are expected to be unobservable with this

593   method unless a subset of modes is driven by an external stimulus, because they are

594   silent in thermodynamic equilibrium.

595   From the exchange asymmetry of the particles in the square pore investigated in

596   Fig. 6 a suggestive picture emerges for driven confined vacancy diffusion (Fig. 7),

597   where the diffusion lengths are confined to the distances from the particle to the direct

598   neighbor cells. Depending on the sign of the asymmetry parameter (Fig. 7a), a small

599   fraction of the particles (blue circles) prefers the direct path towards or away from the

600   active site (red square) at the pore boundary over the path along the boundary to or

601   from the active site. In the center of the wall, the direct path away from the active site

602   to the bulk is preferred over the path along the pore wall when leaving the contact

603   region with the active site (Fig. 7b). But because jumps are allowed in vacancy diffusion

604   only to neighboring cells, the cells belonging to relaxation pool 2 at the wall right and

605   left of the active site 3 must be populated from the bulk 1 by direct jumps form the bulk

606   to the wall. For these jumps, the asymmetry parameter is indeed positive, as observed

607   for the off-center positions of the active site (Fig. 6g). Given the symmetry of the square

608   pore, the in-plane translational diffusion paths resulting from the variation of the

609   asymmetry parameters with the position of the active site on the pore wall demand the

610   existence of eight diffusion vortices inside the planar pore (Fig. 7d). The symmetry of

611   this in-plane translational diffusion pattern matches the symmetry of one of the node

612   patterns of the out-of-plane vibrational modes of a square plate observed by Chladni

613   (Fig. 7e) about a quarter of a millennium earlier (Chladni, 1787). This also suggests

614   that the dynamic of driven vacancy diffusion observed in the computer model reported

615   here is a resonance feature of the pore and thus relates to diffusion eigenmodes. The

616   resonance effect is less pronounced for gas diffusion (Fig. 7c) where the free paths

617   between collisions can span the entire cell. Because the mass flow from relaxation site

618   2 to the active site 3 can be sustained from any position at the pore wall the asymmetry

619   parameter does not need to change sign when the active site moves along the pore

620   wall (Fig. 7e), and the circular paths can have various shapes and can extend across

621   the entire pore, so that the vortex pattern is largely washed out.

622   Given the technological importance of fluid motion in small pores in
623 heterogeneous catalysis (Kärger et al., 2012), it will be interesting to explore, if such
624 correlated motion resulting from standing longitudinal particle-concentration wave
625 patterns near pore walls can be driven by external stimuli like ultrasound, electric or
626 magnetic fields. The standing waves could be enhanced by tuning the driver frequency
627 to the pore resonance like a musician enforces resonance modes on a flute when
628 playing. To enhance the resonance modes, also low-power broad-band, forced
629 oscillations can be considered such as in Fourier transform infrared spectroscopy
630 (Michelson, 1903) and stochastic NMR spectroscopy (Ernst, 1970), while triggering
631 free oscillations by high-power impulses may destroy the porous medium under study.
632
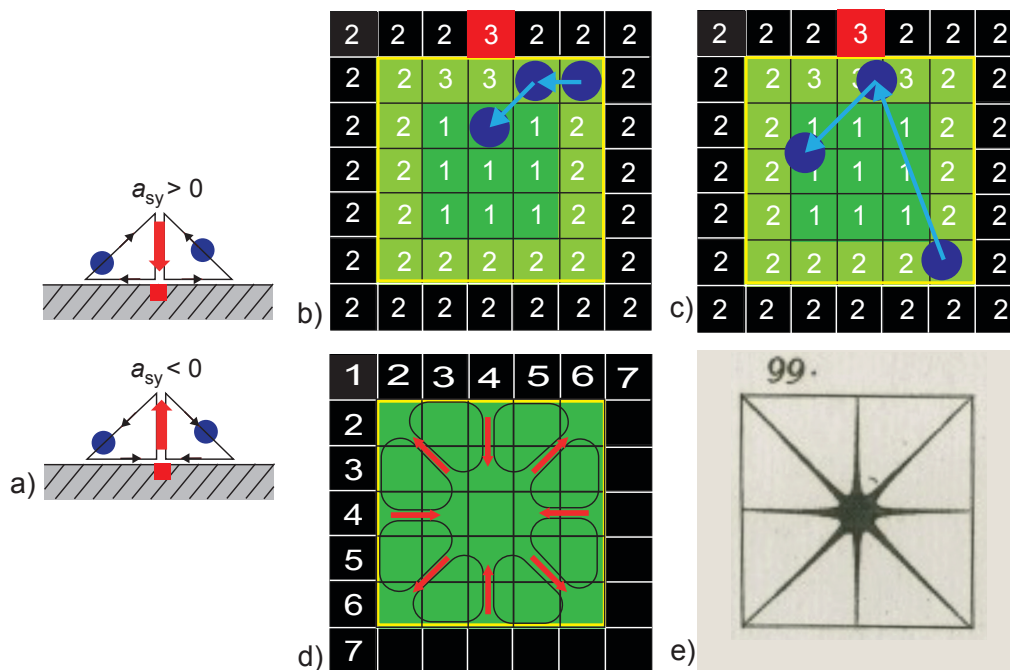
634 Figure 7. Illustration of the exchange asymmetry in driven equilibrium for the square
635 pore of Fig. 6a. a) Depending on the sign of the asymmetry parameter, a small fraction
636 of diffusing particles (blue circles) prefers the direct path towards or away from the
637 active site (red square) at the pore boundary over the path along the boundary from
638 the active site. b) Vacancy diffusion for negative asymmetry parameter and the active
639 site 3 in the center of the pore wall. Jumps are limited to the next nearest cells. The
640 direct path away from the active site to the bulk 1 in the center is preferred over the
641 path along the pore wall 2 when leaving the contact region with the active site. c) Gas
642 diffusion for negative asymmetry parameter and the active site 3 in the center of the
643 pore wall. The free paths between collisions can span the entire cell. d) In-plane
644 translational vacancy-diffusion paths resulting from the variation of the asymmetry
645 parameters with the position of the active site on the pore wall depicted in Fig. 6g. e)
646 Out-of-plane vibrational mode of a square plate observed by Chladni (Chladni, 1787).
647

5. Summary

The evidence provided by Monte Carlo simulations of random particle jumps on a 2D checkerboard and by simulations of 2D gas diffusion with topological confinements supports the notion, that asymmetry in three-site exchange maps reports the non-Brownian diffusion dynamics of confined particles in driven equilibrium. Depending on the sign of the asymmetry parameter, a small fraction of all particles prefers the direct path towards or away from the active site at the pore boundary over the path along the boundary to or from the active site resulting in a circular flux (Fig. 7). Both, driven vacancy diffusion and driven gas diffusion produce congruent results. These are: 1) Circular exchange is a manifestation of driven equilibrium and leads to asymmetry of exchange peaks, while thermodynamic equilibrium manifests itself in detailed balance and symmetry of exchange peaks. 2) The circular exchange in driven equilibrium appears to be a resonance phenomenon which can potentially be driven by external stimuli. Yet, the reported simulations are limited to two dimensions, and it may be argued that the asymmetry of exchange vanishes in the more common pores with three spatial dimensions. But two-dimensional diffusion is not an abstract model and arises for gas atoms adsorbed to metal surfaces (Oura et al., 2013), so that the driven coherent particle diffusion indicated by the non-zero asymmetry parameter may be observed there. Given the congruent simulation evidence for driven vacancy diffusion and gas diffusion in two-dimensional confinements it is hypothesized, that confined diffusion can be partially converted to coherent motion by external excitation so that detailed balance will be violated as observed in nonequilibrium phenomena (Gnesotto et al. 2018, Lynn et al. 2021).

Author Contributions

BB posed the question, executed the simulations of confined vacancy diffusion, and wrote the manuscript. MA worked out the algorithm for vacancy diffusion along with BB and supervised MP. MP programmed the algorithm for confined gas diffusion and executed the gas-diffusion simulations.

Acknowledgement

BB thanks Thomas Wiegand at RWTH Aachen University for stimulating discussions, hosting him as a PostProf, and access to the computing facilities. He also thanks Ilya Kuprov for his flash of inspiration on linking three-site exchange to Fick's second law

at a random EUROMAR 2022 breakfast encounter and Stephan Appelt, Gerd Buntkowsky, Jeffrey Reimer, and Tom Barbara for stimulating discussions. Special thanks go to the unknown reviewer who commented on the manuscript (Gao and Blümich, 2020), that asymmetry in three-site exchange violates the principle of detailed balance and to the anonymous reviewer of this manuscript who educated the authors on the intricacies of Monte Carlo simulations.

Code availability

The codes for simulating confined 2D vacancy diffusion and confined 2D gas diffusion are reported in the supplement.

Conflict of Interest statement

Other than that BB is on the advisory board of Magnetic Resonance the authors declare no conflict of interest.

References

Bialynicki-Birula, I. and Bailynicky-Birula, I., Modeling Reality, Oxford University Press, Oxford, 2004.

Björgvinsdóttir, S., Moutzouri, P., Walder, B. J., Matthey, N., and Emsley, L., Hyperpolarization transfer pathways in inorganic materials, J. Magn. Reson. 323, 106888, 2021.

Brownstein, K.R. and Tarr, C. E., Spin-Lattice Relaxation in a System Governed by Diffusion, J. Magn. Reson. 26, 17–24, 1977.

Bunde, A., Caro, J., Kärger, J., and G. Vogel, eds., Diffusive Spreading in Nature and Technology, Springer Nature, Cham, 2018.

Bytchenkoff, D., and Rodts, S., Structure of the two-dimensional relaxation spectra seen within the eigenmode perturbation theory and the two-site exchange model, J. Magn. Reson. 208, 4–19, 2011.

Callaghan, P. T. and Stepišnik, J., Modulated Gradient NMR, J. Magn. Reson. 117, 118–122 (1995).

Callaghan, P.T., Translational Dynamics and Magnetic Resonance: Principles of Pulsed Gradient Spin Echo NMR, Oxford University Press, Oxford, 2011.

Chladni, E. F. F., Entdeckungen über die Theorie des Klanges, Leipzig, Weidmanns Erben und Reich, 1787.

716 de Hoop, A.T. and Prange, M.D., Variational analysis of the natural decay rates and
717 eigenmodes of cavity-enclosed diffusive fields, J. Phys. A: Math. Theor. 40, 12463–
718 12477, 2007.

719 Einstein, A., Zur Quantentheorie der Strahlung, Physikalische Zeitschrift 18, 121–128,
720 1917.

721 Ernst, R. R., Bodenhausen, G., and Wokaun, A., Principles of Nuclear Magnetic
722 Resonance in One and Two Dimensions, ClarendonPress, Oxford, 1987.

723 Ernst, R. R., Magnetic Resonance with Stochastic Excitation, J. Magn. Res. 3, 10–27,
724 1970.

725 Feynman, R., Leighton, R. B., and Sands, M., The Feynman Lectures on Physics, vol.
726 1, chapter 46, Addison-Wesley, Reading, Fourth Printing, 1966

727 Fick, A., Ueber Diffusion, Annalen der Physik 94, 59–86, 1855.

728 Gao, Y., and Blümich, B., Analysis of three-site T_2-T_2 exchange NMR, J. Magn. Reson.
729 315, 106740, 2020.

730 Gnesotto, F. S., Mura, F., Gladrow, J., and Broedersz, C. P., Broken detailed balance
731 and non-equilibrium dynamics in living systems: a review, Rep. Prog. Phys. 81,
732 066601, 2018.

733 Grebenkov, D. S., A fast random walk algorithm for computing the pulsed-gradient
734 spin-echo signal in multiscale porous media, J. Magn. Reson. 208, 243–255, 2011.

735 Grebenkov, D. S. and Nguyen, B.-T., Geometrical Structure of Laplacian
736 Eigenfunctions, SIAM Review 55, 601–667, 2013.

737 Han, S.-I. and Blümich, B., Two-dimensional representation of position, velocity, and
738 acceleration by PFG-NMR, Appl. Magn. Res. 18, 101–114, 2000.

739 Hughes, B. D., Random Walks and Random Environments, Clarendon Press, Oxford,
740 1995.

741 Jeener, J., Meier, B. H., Bachmann, P., and Ernst, R. R., Investigation of exchange
742 processes by two-dimensional NMR spectroscopy, J. Chem. Phys. 71 4546–4553,
743 1979.

744 Kärger, J., Ruthven, D. M., and Theodorou, D. N., eds., Diffusion in Nanoporous
745 Materials, vol. 1, Wiley-VCH, Weinheim, 2012.

746 Kundt, A., Über eine neue Art akustischer Staubfiguren und über die Anwendung
747 derselben zur Bestimmung der Schallgeschwindigkeit in festen Körpern und Gasen,
748 Annal. Phys. Chem. 203, 497–523, 1866.

Kuprov, I., private communication with BB at the EUROMAR 2022 conference in Utrecht, July 10–14, 2022.

Boltzmann, L., Weitere Studien über das Wärmegleichgewicht unter Gasmolekülen, Sitzungsber. Kais. Akad. Wiss., Wien, Math, Natruwiss. Classe 66, 275-370, 1872.

Lacabanne, D., Wiegand, T., Di Cesare, M., Orelle, C., Ernst, M., Jault, J.-M., Meier, B.H., and Böckmann, A., Solid-State NMR Reveals Asymmetric ATP Hydrolysis in the Multidrug ABC Transporter BmrA, J. Am. Chem. Soc. 144, 12431–12442, 2022.

Lee, J.-H., Labadie, C., Springer Jr., C. S., and Harbison G.S., Two-Dimensional Inverse Laplace Transform NMR: Altered Relaxation Times Allow Detection of Exchange Correlation, J. Am. Chem. Soc. 115, 7761–7764, 1993.

Lynn, C. W., Cornblath, W. J., Papadopoulos, L., Bertolerod, M. A., and Bassett, D. S., Broken detailed balance and entropy production in the human brain, PNAS 118, e2109889118, 2021.

Maxwell, J. C., On the dynamical theory of gases, Philos. Trans. R. Soc. London 157 49–88, 1867.

McDonald, P. J., Korb, J.-P., Mitchell, J., and Monteilhet, L., Surface relaxation and chemical exchange in hydrating cement pastes: A two-dimensional NMR relaxation study, Phys. Rev. E 72, 011409, 2005.

Metropolis, N., Rosenbluth, A.W., Rosenbluth, M.N., Teller, A.H., and Teller, E., Equation of State Calculations by Fast Computing Machines, J. Chem. Phys. 21, 1087–1092, 1953.

Michel, M., Kapfer S. C., and Krauth, W., Generalized event-chain Monte-Carlo: Constructing rejection-free global-balance algorithms from infinitesimal steps, J. Chem. Phys. 140 054116, 2014.

Michelson, A. A., Light Waves and Their Uses, The University of Chicago Press, Chicago, 1903.

Müller, N. and Jerschow, A., Nuclear Spin Noise Imaging, PNAS 103, 6790–6792, 2005.

Olaru, A. M., Kowalski, J., Sethi, V., and Blümich, B., Exchange relaxometry of flow at small Péclet numbers in a glass bead pack, J. Magn. Reson. 220, 32–44, 2012.

Onsager, L., Reciprocal Relations in Irreversible Processes, Phys. Rev. 37, 405-426, 1931.

Oura, K., Lifshits, V. G., Saranin, A. A., Zotov, A. V., and Katayama, M., Surface Science: An Introduction, Springer, Berlin, 2013, chapter 13.

783 Parsons, E. C., Does, M. D., and Gore J.C., Temporal Diffusion Spectroscopy: Theory

784 and Implementation in Restricted Systems Using Oscillating Gradients, Magn. Reson.

785 Med. 55, 75–84, 2006.

786 Reviewer 2023, anonymous reviewer of Blümich, B., Parziale, M., and Augustine, M.,

787 Monte-Carlo Analysis of Asymmetry in Three-Site Relaxation Exchange: Probing

788 Detailed Balance, Magnetic Resonance Preprint, 2023, doi.org/10.5194/mr-2023-8.

789 Sabelfeld, K. K., Monte Carlo Methods in Boundary Value Problems, Springer-Verlag,

790 Berlin, 1991.

791 Sandstrom, J., Dynamic NMR Spectroscopy, Academic Press, Cambridge, MA, 1983

792 Schlagnitweit, J. and Müller, N., The first observation of Carbon-13 spin noise spectra,

793 J. Magn. Reson. 224, 78–81, 2012.

794 Seitz, F., On the Theory of Vacancy Diffusion in Alloys, Phys. Rev. 74, 1513–1523,

795 1948.

796 Sleator, T., Hahn, E.L., Hilbert, C., and Clarke, J., Nuclear Spin Noise, Phys. Rev. Lett.

797 55, 1742–1745, 1985.

798 Song, Y. Q., Detection of the High Eigenmodes of Spin Diffusion in Porous Media,

799 Phys. Rev. Lett 85, 3887–3881, 2000.

800 Song, Y.-Q., Venkataraman, L., Hürlimann, M. D., Flaum, M., Frulla, P., and Straley,

801 C., T_1-T_2 Correlation Spectra Obtained by Using a Fast Two-Dimensional Laplace

802 Inversion, J. Magn. Reson. 154, 261–268, 2002.

803 Stepišnik, J., Mohoric, A., Lahajnar, G., Mattea, C., Stapf, S., and Sersa, I., Velocity

804 autocorrelation spectra in molten polymers measured by NMR modulated gradient

805 spin-echo, Europhysics Lett. 106, 27007, 2014.

806 Torrey, H. C., Bloch Equations with Diffusion Terms, Phys. Rev. 104, 563–565, 1956.

807 Valiullin, R., ed., Diffusion NMR of Confined Systems, R. Soc. Chem., Cambridge,

808 2017.

809 van Kampen, N. G., Stochastic Processes in Physics and Chemistry, Elsevier,

810 Amsterdam, 1992.

811 Van Landeghem, M., Haber, A., d'Espinose de Lacaillerie J.-B., and Blümich, B.,

812 Analysis of Multisite 2D Relaxation Exchange NMR, Concepts Magn. Reson. 36A,

813 153–169, 2010.

814 Wolf-Gladrow, D. A., Lattice-Gas Cellular Automata and Lattice Boltzmann Models,

815 Springer, Berlin, 2000.